Article

Designing of High-Performance MnNiS@MXene Hybrid Electrode for Energy Storage and Photoelectrochemical Applications

Maqsood Ahmad [1], Muhammad Imran [1], Amir Muhammad Afzal [1,*], Muhammad Ahsan ul Haq [1], Areej S. Alqarni [2], Muhammad Waqas Iqbal [1], Shams A. M. Issa [3] and Hesham M. H. Zakaly [4,5,6]

[1] Department of Physics, Riphah International University, Campus Lahore, Lahore 54000, Pakistan; maqsoodahmad0809@gmail.com (M.A.); m.imransharif24@gmail.com (M.I.); m_a.haq@yahoo.com (M.A.u.H.); waqas.iqbal@riphah.edu.pk (M.W.I.)
[2] Department of Physics, College of Science, Princess Nourah Bint Abdulrahman University, P.O. Box 84428, Riyadh 11671, Saudi Arabia; arsalqarni@pnu.edu.sa
[3] Physics Department, University of Tabuk, Tabuk 47512, Saudi Arabia; shams_issa@yahoo.com
[4] Institute of Physics and Technology, Ural Federal University, 620002 Yekaterinburg, Russia; h.m.zakaly@gmail.com
[5] Computer Engineering Department, Faculty of Engineering and Natural Sciences, Istinye University, Istanbul 34396, Turkey
[6] Department of Physics and Technical Sciences, Western Caspian University, Baku AZ1072, Azerbaijan
* Correspondence: amirafzal461@gmail.com

Abstract: The overconsumption of fossil fuels is leading to worsening environmental damage, making the generation of clean, renewable energy an absolute necessity. Two common components of electrochemical energy storage (EES) devices are batteries and supercapacitors (SCs), which are among the most promising answers to the worldwide energy issue. In this study, we introduce an exceptionally efficient electrode material for supercapacitors, composed of a hydrothermally synthesized composite known as MnNiS@MXene. We utilized XRD, SEM, and BET to analyze the material's crystallinity, morphology, and surface area. The Qs of MnNiS@MXene was a remarkable 1189.98 C/g or 1983.3 F/g at 2 A/g under three electrode assemblies in 1 M KOH electrolyte solution. Activated carbon was used as the negative electrode, while MnNiS@MXene served as the positive electrode in the assembled supercapattery device (MnNiS@MXene//AC). This device showed exceptional performance, a specific capacity of 307.18 C/g, a power density of 1142.61 W/kg, and an energy density of 34.79 Wh/kg. Additionally, cyclic durability was evaluated through 7000 cycles of charging/discharging, demonstrating that it maintained approximately 87.57% of its original capacity. The successful integration of these materials can lead to electrodes with superior energy storage capabilities and efficient photoelectrochemical performance. The aforementioned findings suggest that MnNiS@MXene exhibits promising potential as an electrode material for forthcoming energy storage systems.

Keywords: supercapattery; manganese nickel sulfide; MXene; photochemical activity; energy storage

1. Introduction

The increasing scarcity of fossil fuels, escalating pollution levels, and the phenomenon of climate change have collectively prompted a heightened pursuit of sustainable and renewable resources [1,2]. The need to save the environment and lessen dependency on fossil fuels has increased dramatically [3–6]. As wind and solar power usage grows and electric and hybrid car technology advances, sustainable energy generation and storage solutions become more essential [7–12]. Batteries and supercapacitors, two types of energy storage technology, have attracted a lot of attention in this regard. Supercapacitors are distinguished by their long cycle life (>10,000 cycles), high power density, simple operating principles, and quick charge/discharge speeds [13–16]. Supercapacitors are a significant

advancement over conventional dielectric capacitors, even if their energy density normally ranges between 0.5 and 10 Wh kg^{-1}, which is still less than that of standard batteries, which typically have energy densities of 125 to 175 Wh kg^{-1} for lithium-ion batteries [17–20].

It is critical to improve these energy storage technologies to meet the problems presented by the depletion of fossil fuels, environmental degradation, and the pressing need for sustainable energy alternatives [21,22]. It is still necessary to connect batteries or other power sources [23,24]. Supercapacitors are particularly notable for their remarkably fast energy storage [25–27]. SCs store energy due to the fact that electrolyte ions are adsorbed, and electrical double layers are created on the electrode surface [28,29]. Due to an external voltage, the second technique relies on rapid and reversible surface redox reactions between the electrolyte ions and electrode material [30–32]. Low energy density is a major challenge for supercapacitors. Their application in many industries is severely limited by this constraint [33–35]. To increase the number of applications and range of supercapacitors, research and development efforts are still focused on finding a solution to this energy-density problem [36,37].

A supercapattery is a novel approach that fills the gap between batteries and supercapacitors [38,39]. Supercapatteries are an effective and adaptable energy storage solution for a variety of applications because they combine the high energy density of batteries with the high power density and quick charge/discharge times of supercapacitors [40,41]. Considering that the electrochemical performance of SCs is greatly influenced by the characteristics of the electrode materials, for supercapattery technology, choosing the right electrode materials is essential, with kinetic characteristics being the most vital aspect to take into account [42]. The selection of electrode material is based on several key characteristics including outstanding electrocatalytic performance, stability, high surface area, pore volume, and electrical conductivity [14,16,43–46].

For usage as electrode materials in supercapattery technology, a range of materials with high capacitance values, simplicity of synthesis, availability, and environmental friendliness has been investigated in light of these factors [47,48]. Unfortunately, a number of these materials have drawbacks including a low volume capacity and problems with material combination, particularly with carbon-based materials and oxides of different metals [49–51]. In this regard, transition metal sulfides have garnered a lot of interest across several disciplines. They are a plentiful and reasonably priced class of materials that occur naturally in minerals including chalcocite (Cu_2S), heazlewoodite (Ni_3S_2), and pyrite (FeS_2). One essential ingredient in these sulfides, sulfur, has several possible valence states, providing a significant theoretical capability. As electrode materials, transition metal sulfides have many benefits such as superior electrochemical performance, cheap manufacturing costs, easy accessibility, and environmentally friendly techniques. These characteristics make them extremely capable for a variety of uses.

Transition metal sulfides (TMSs) can be found in layered or non-layered materials, depending on their structural makeup [52–54]. One of the three covalently bound layers of S-M-S particles in MoS_2, SnS_2, VS_2, WS_2, and other layered metal sulfides is held in place by van der Waals forces of attraction. Conversely, non-layered TMSs such as Mn-Sx, Cox-S, and Nix-S have benefits like inexpensive raw material costs, easy manufacture, high theoretical capacitance, and multiple oxidation states [55,56]. Potential electroactive materials such as $Ni_xCo_xS_x$, $Ni_xMo_xS_x$, $Zn_xCo_xS_x$, $Co_xFe_xS_x$, and $Ni_xMn_xS_x$ are being studied, and their compositions show promise for energy storage applications [57]. The project's goal is to enhance the development of supercapacitors and rechargeable batteries in hybrid electric energy storage (EES) systems [58,59].

A novel class of two-dimensional (2D) transition metal carbide, nitride, and carbonitride materials is MXenes. Their distinct structural features have garnered significant attention in recent times. The strong mechanical structure, excellent electrical conductivity, and electrochemical stability of methylenes are characteristics that set them apart [60–62]. These characteristics distinguish them as exceptional two-dimensional materials, notably in the context of supercapacitor applications when utilized as scaffolds for the synthesis

of nanocomposite electrodes [63]. Moreover, composite electrodes perform much better electrochemically when 2D conductive MXenes are added. This enhancement is attributed to both the additional electroactive sites provided by the electrode structure and its overall better electrical conductivity [64–67].

Motivated by the noteworthy advantages offered by MXene and manganese nickel sulfide, we created a battery-grade electrode employing MXene and manganese nickel sulfide that was generated hydrothermally for an asymmetric energy storage device called a supercapattery. This unique electrode performs well with a 34.79 Wh/kg energy density, 1142.61 W/kg power density, 307.18 C/g specific capacity, 81.93% coulomb efficiency, and 87.57% capacity retention after 7000 GCD cycles. Asymmetric energy storage devices can operate more efficiently with our findings.

2. Results and Discussion

Figure 1A shows the final product dried for 12 h at 60 °C in a vacuum oven. To produce MnNiS@MXene hybrids, the ideal concentrations of previously produced MXene and MnNiS progenitors were dissolved in water using ultrasonication and then introduced to the hydrothermal autoclave. Pre-synthesized AgCoS nanoparticles were combined with MXene to create the MnNiS@MXene composite material. AgCoS (mass ratio: 50%) and MXene (mass ratio: 50%) were utilized in the composite. After being repeatedly rinsed with ethanol and deionized water, the resulting precipitates were centrifuged using deionized water to remove any remaining unreacted components. Figure 1B shows the product dried in a vacuum oven at 60 °C for 12 h.

2.1. Characterizations

Utilizing X-ray diffraction (XRD) and scanning electron microscopy (SEM) for surface morphology research, the crystalline characteristics of manganese nickel sulfide were investigated. The material's successful synthesis was confirmed by employing these techniques. Each sample showed a high degree of crystallinity, as shown by the narrow width of the principal X-ray diffraction (XRD) peaks. The NiS (JCPDS# 71-1682) crystal faces (311), (100), and (111) were identified by the diffraction peaks at 38.31°, 52.03°, and 70.51°, respectively. Crystal faces (002) and (212), respectively, were responsible for the diffraction peaks at 48.3° and 64.38° in the MnS (JCPDS40-1289) sample. Synthesized MnNiS, a transition bimetallic sulfide, displayed molecular configurations similar to those of MnS and NiS. The additional diffraction peaks at 18.91, 46.5°, and 71.35° of MnNiS@MXene corresponded to (002), (102), and (150), a crystal face of MXene. The results indicated that MnNiS@MXene contained the diffraction peaks of MXene and MnNiS. Further evidence for the successful synthesis and existence of crystalline minerals was provided by the XRD patterns of the MAX phase and MXene, which were consistent with ICDD No. 00-052-0875 [68] as shown in Figure 2a. Figure 2b shows a comparison of the scanning electron micrographs taken of MXene nanosheets and the MnNiS@MXene composite. There was a consistent distribution of the layered structure of MnNiSx@MXene. In the interlayers and on the surface of MXene, MnNiS, which looks like a coral flower, was crystallized without obvious agglomeration and showed heterogeneous nucleation. The mutualism of Ni^{2+} and Mn^{2+} produced the structure of MnNiS, which resembled a coral flower. Using the Scherrer equation, we were able to calculate the crystalline size of the synthesized nanostructure [40,69].

$$D = \frac{K\lambda}{\beta\cos(\theta)}$$
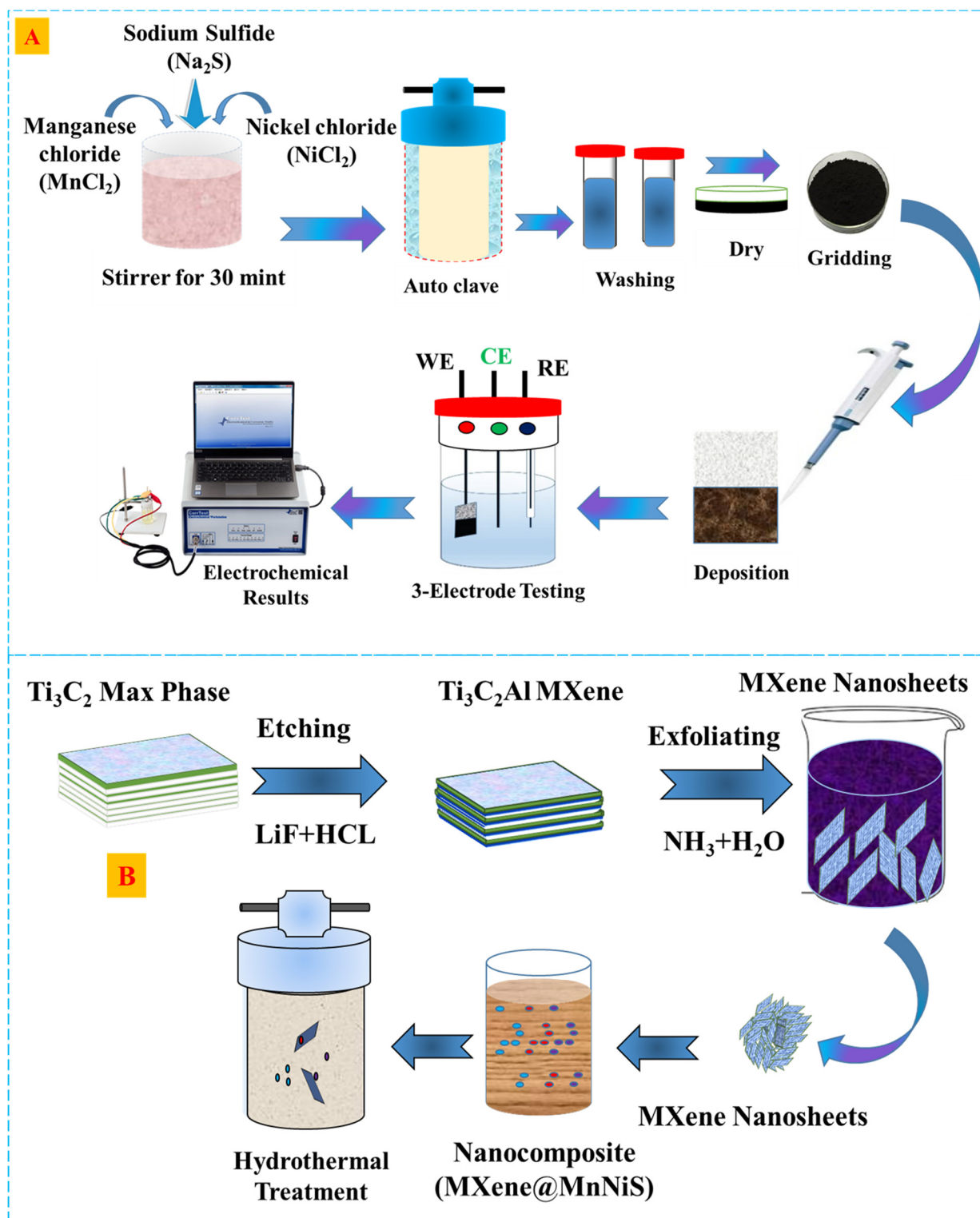
Figure 1. (**A**) Systematic depiction of a hydrothermal method for synthesizing manganese nickel sulfide and potentiostat measurements. (**B**) A synthesis process of the MnNiS@MXene nanocomposite electrode material.
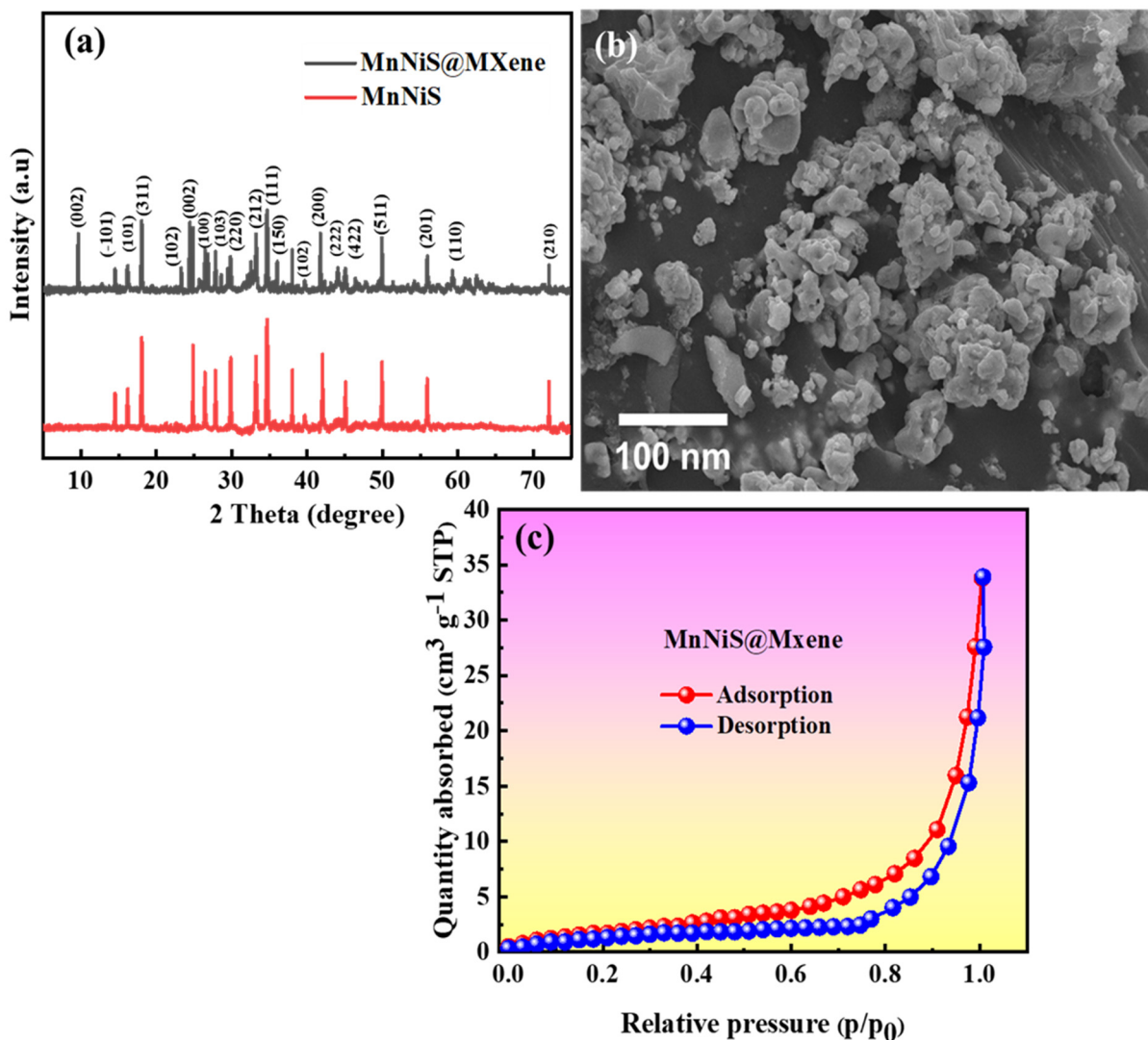
Figure 2. (**a**) XRD patterns of MnNiS and MnNiS@MXene. (**b**) SEM image of the nanocomposite material MnNiS@MXene. (**c**) N_2 adsorption–desorption isotherms.

In this case, β describes the total width at half maximum, while λ stands for the X-ray wavelength, which was 1.59 Å. In this instance, the constant term K was given as 0.94. MnNiS@MXene had a specific surface area that was four times larger than that of MXene and eight times larger than that of MnNiS. Therefore, MnNiS@MXene is a mesoporous material with pores that range in size from 3 to 20 nm.

In addition, MnNiS@MXene had somewhat larger pores and a little larger volume than MnNiS and single MXene. As depicted in Figure 2c of the BET study, the combined influence of MXene and MnNiS resulted in an augmentation of the composite's specific surface area and an enrichment of its pore channels.

2.2. Electrochemical Findings

The electrochemical performance of synthetic materials was assessed using a comprehensive series of tests, employing a three-electrode configuration. After the initial evaluation, cycle voltammetry (CV) was conducted using an electrolyte containing 1 molar of potassium hydroxide (KOH) at a fixed potential of 0–0.6 V. The CV examination identified crucial material properties. Figure 3a–c displays the CV curves obtained at scan rates ranging from 5 to 60 mV/s. The study validated previous research indicating that the materials created possess battery-like properties, characterized by different redox peaks mostly associated with the interface between the OH- ions and electrode material.

Differentiable redox peaks are essential markers of the electrochemical reactions occurring in battery-grade electrodes during cyclic voltammetry (CV). The oxidation and reduction processes of the active components in the battery electrode are represented by these peaks. Comprehending these peaks facilitates the evaluation of the battery materials' performance, stability, and efficiency. In Figure 3d, the CV's of the MXene, MnNiS, and MnNiS@MXene composite are compared at a scan rate of 5 mV/s. The findings of the experiments indicate that MnNiS@MXene exhibits superior electrochemical characteristics compared to MXene and manganese nickel sulfide in standalone.
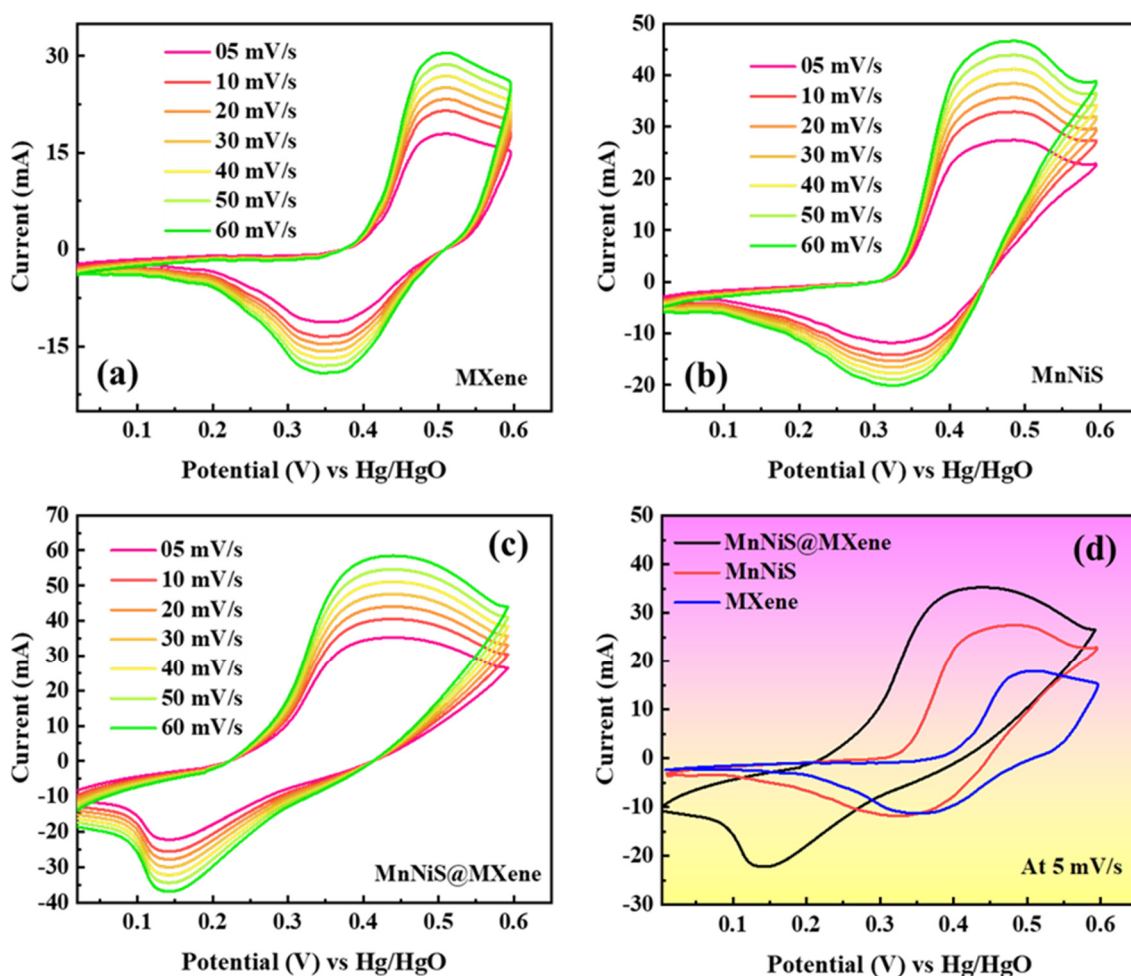

Figure 3. Depiction of the CV of (**a**) MXene, (**b**) MnNiS, and (**c**) MnNiS@MXene composite. (**d**) The CV evaluation of the MXene, MnNiS, and MnNiS@MXene composite at a scan rate of 5 mV/s.

Furthermore, a galvanostatic charge–discharge (GCD) test was conducted using a 1 molar potassium hydroxide (KOH) electrolyte. The GCD curves of MXene, MnNiS@MXene, and manganese nickel sulfide are depicted in Figure 4a–c. In Figure 4d, the MXene, MnNiS, and MnNiS@MXene nanocomposite of GCD are compared at a current density of 2.5 A/g. The galvanostatic charge–discharge (GCD) curves deviated from the expected triangular shape, indicating nonlinearity. This deviation, representing redox reactions occurring at the electrode surface, suggests that the synthesized materials are suitable for use as battery-quality electrode materials. As the current density increases, the charge/discharge duration decreases. However, the curves maintained a consistent pattern, demonstrating the durability of the synthetic materials. The reduction in discharge times was due to the decrease in electrode-specific capacities and shorter contact times at higher current densities.
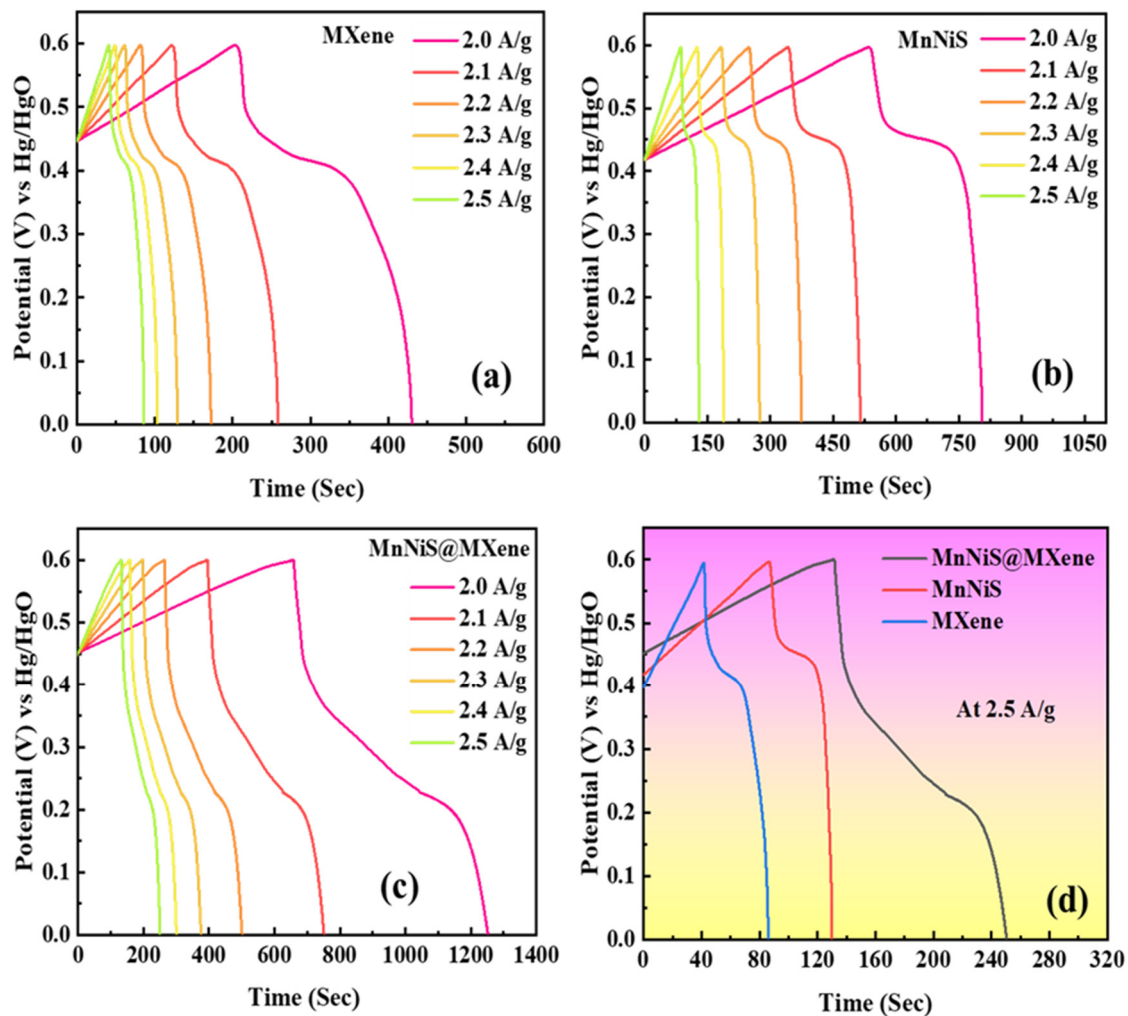
Figure 4. (**a**) Illustration of the GCD of the MXene, (**b**) MnNiS, and (**c**) MnNiS@MXene composite. (**d**) A comparative analysis of the GCDs of the MXene, MnNiS, and MnNiS@MXene composites at 2.5 A/g are presented.

The MnNiS@MXene material showed exceptional rate capabilities at a 5 mV/s scan rate with a specific capacity of 956.77 C/g. Still, the specific capacity gradually decreased as the scan speeds rose because of the shorter contact time. Figure 5a compares the specific capacities of MXene, MnNiS, and MnNiS@MXene at a scan rate of 5 mV/s. The following formula was used to obtain each sample of precise capacity values.

$$Qs = \frac{1}{mv} \int_{Vi}^{Vf} (I \times V) dV \tag{1}$$

Equation (1) denotes the Qs (specific capacity), while the integral $\int_{Vi}^{Vf} (I \times V) dV$ represents the integral of the curve. The active mass (m) and scan rate (V) are variables in this equation. The Qs of MXene and manganese nickel sulfide were determined using Equation (1), yielding a Qs of 646.91 C/g and 748.01 C/g, respectively. Figure 5a shows that the Qs of MnNiS@MXene was remarkably higher than that of MXene and MnNiS, reaching an amazing 956.77 C/g at a scan rate of 5 mV/s. Figure 5b presents comparisons based on the galvanostatic charge–discharge (GCD). The results of this comparison clearly show that the sample that performed the best had the same weight ratio of MXene to manganese nickel sulfide. Its superior electrochemical performance was shown over an extended discharge period in comparison to MXene and manganese nickel sulfide separately. The great high-rate capacity is further highlighted by the GCD curve's consistent form, even

at increasing current densities. The formula provided can be utilized to derive specific capacity values.

$$Q = \frac{I \times \Delta t}{m} \tag{2}$$

The above equation gives the specific capacity, where "m" is the active mass and "Δt" is the discharging time. The specific capacities of MXene and manganese nickel sulfide were found to be 450 C g^{-1} and 542.9 C g^{-1}, respectively, when Equation (2) was used. The MnNiS@MXene composite outperformed expectations, as seen by the GCD studies, with an amazing specific capacity of 1189.98 C/g, as illustrated in Figure 5b. These findings show that the composite of manganese nickel sulfide and MXene is more electroactive than the two elements combined, which allows ions and electrons to move more easily.
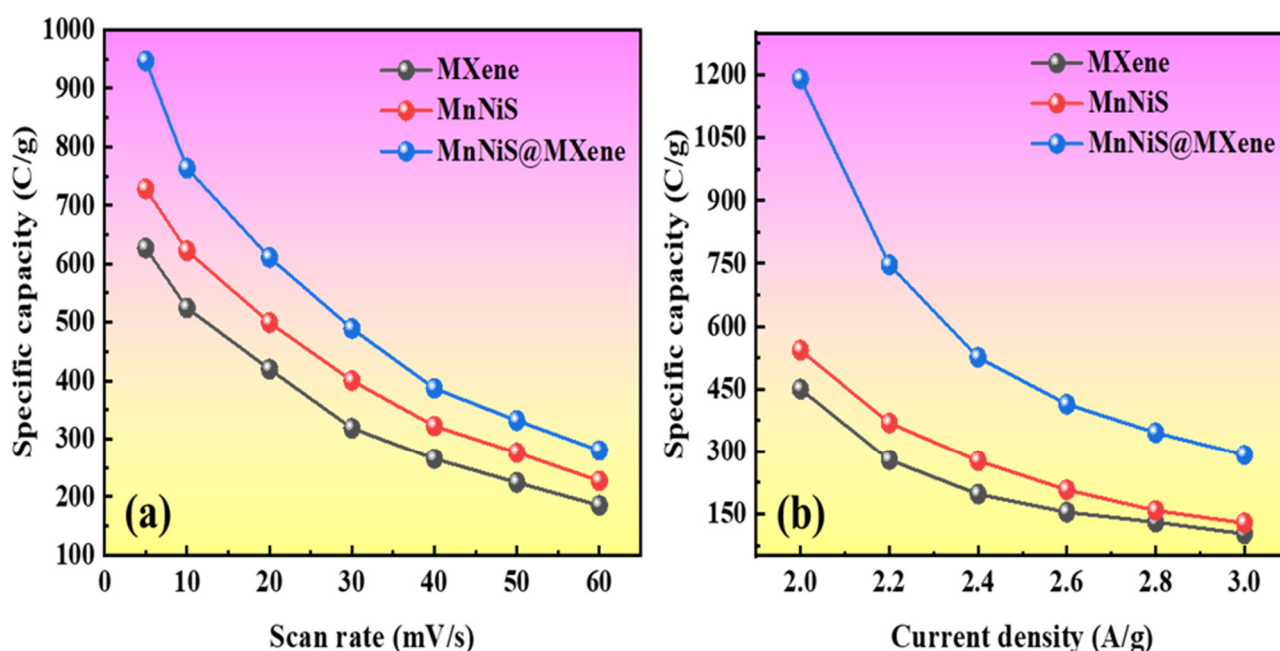

Figure 5. (**a**) Comparison of the MXene, MnNiS, and MnNiS@MXene specific capacity values at various scan rates and (**b**) current densities.

The specific capacity decreased rapidly with the increase in scan rates and current densities in the supercapattery primarily due to kinetic limitations, mass transport limitations, and increased electrical resistance [70]. These factors collectively led to the incomplete utilization of the active material, reduced charge transfer, and lower overall efficiency of the electrochemical processes [71]. All things considered, the thorough characterizations carried out on electrodes provide credence to the finding that MnNiS@MXene demonstrates remarkable electrochemical presentation, indicating that it would be a good choice for anode material in a supercapattery. The stability under a three-electrode assembly by the CV curve of the composite electrode (MnNiS@MXene) before and after 7000 cycles is shown in Figure S1a. The cyclic performance measured by GCD before and after 7000 cycles is represented in the Supplementary Materials (Figure S1b). Capacity retention of the composite electrode (MnNiS@MXene) was 88% after 7000 cycles, as shown in Supplementary Materials Figure S1c.

2.3. Supercapattery Characterization

In the supercapattery configuration, the activated carbon electrode received a negative potential, while the MnNiS@MXene electrode received a positive potential. The supercapattery electrode's charge storage mechanism combined the faradaic reactions of batteries with the electrostatic storage of supercapacitors and employed MnNiS@MXene composite

materials and techniques to provide high energy and power densities with an extended cycle life.

Figure 6a shows a simplified diagram of the two-electrode setup. The CV evaluation between the two electrodes used in the supercapattery device is shown in Figure 6b. Activated carbon's capacitive nature is demonstrated by the constant slope observed during cyclic voltammetry (CV). Conversely, the conspicuous peaks observed in the CV of MnNiS@MXene indicate it as a battery-grade material.
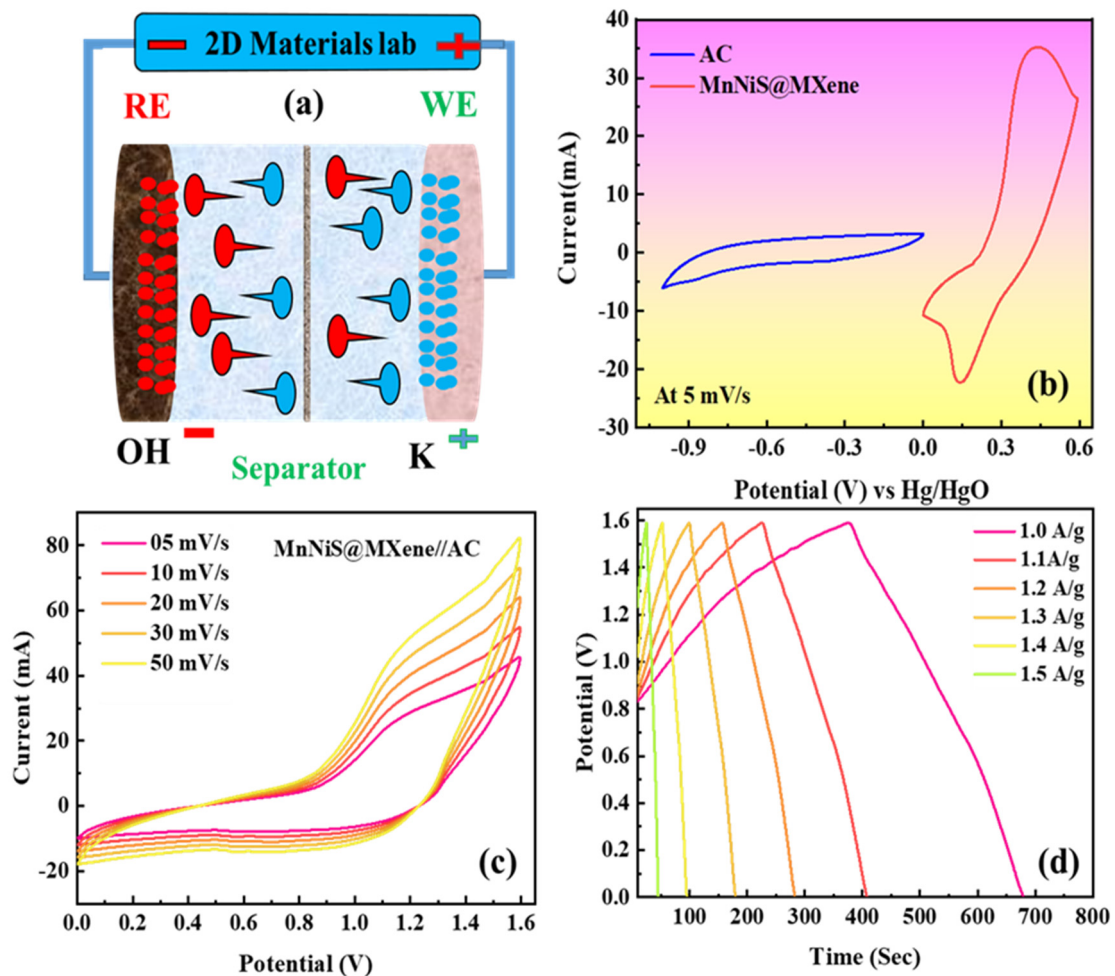

Figure 6. (**a**) A diagram showing the two-electrode setup, (**b**) the CV of a real device at different scan rates, (**c**) the GCD at various current densities, and (**d**) the GCD curves of the supercapattery at different current densities.

The initial stage in the characterization procedure was to use cyclic voltammetry to determine the best potential window, which ranged from 0 V to 1.6 V. It was observed that the device's optimal potential window was 0 to 1.6 V. Next, GCD and CV were used to evaluate the device's performance. Before characterization, each electrode was conditioned within its potential window. Figure 6c depicts the CV at 5–50 mV/s across 0–1.6 V. The device's CV response varied dramatically between the battery-grade and carbonaceous electrodes. The hybrid CV form indicates that energy was stored by diffusion and surface control.

A supercapattery shows the characteristics of both a battery and capacitor in their cyclic voltammetry (CV), and different redox peaks may be seen as a result of faradaic processes. No peaks indicated charge accumulation via adsorption at lower potentials. A diffusion-controlled charge storage mechanism was shown by modest peaks at higher potentials. As indicated in Figure 6d, GCD was performed at various current densities

from 0 V to 1.6 V. The GCD profiles were neither hump-shaped nor triangular, showing that surface-controlled and diffusion-controlled mechanisms affect the charge storage.

The specific capacity was calculated using the following formula, with the GCD curves serving as a reference:

$$Qs = \frac{I \times \Delta t}{m} \tag{3}$$

The specific capacity of the real device at different current densities is depicted in Figure 7a. At a current density of 1.1 A/g, the device achieved its maximum specific capacity of 307.18 C/g. The device was examined using the electrochemical impedance spectroscopy (EIS) technique. Figure 7b illustrates the experimental findings, demonstrating the high electroactivity of the device and its facilitation of enhanced ion and electron mobility.
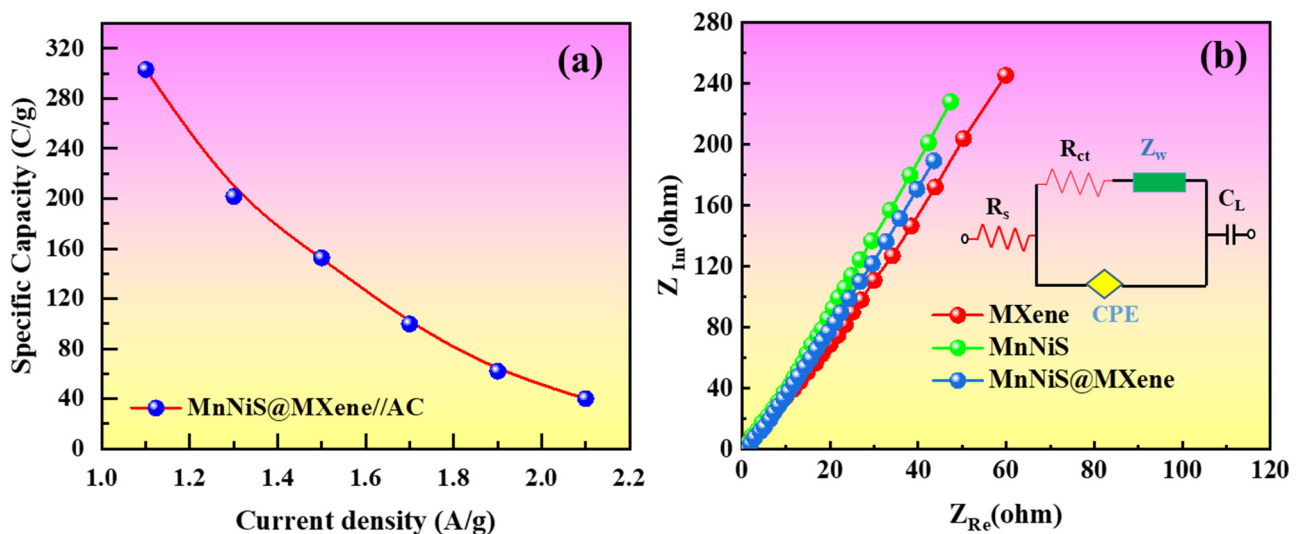

Figure 7. (**a**) The specific capacity of the real device. (**b**) Analysis of the EIS for MXene, MnNiS, and MnNiS@MXene with an equivalent circuit.

A vertical EIS curve, which represents the ideal capacitor behavior, is ideal. However, in this case, the battery-like properties of the materials mean that the curve form was not vertical [45]. The charge transfer resistance is represented by the semi-circle, and the x-intercept of the curve offers an estimate of the series resistance at higher frequencies. The MnNiS@MXene electrode showed a lower series resistance value than the MnNiS and MXene electrodes, according to an analysis of the EIS data, suggesting a superior electrical conductivity for MnNiS@MXene. Therefore, based on these findings, it can be concluded that MnNiS@MXene exhibits greater potential as a viable option for practical applications that demand high electrical conductivity.

To evaluate the stability of the device, it underwent a comprehensive series of 7000 consecutive charging and discharging cycles, employing a current density of 1.15 A/g. The stability test results showed that even after 7000 cycles, the device still held 88.05% of its capacity. The charging and discharging efficiencies differed from one another, but their ratio essentially remained constant, as shown in Figure 8a. In contrast, the capacity retention and columbic efficiency after several cycles are depicted in Figure 8b. The columbic efficiency and capacity retention of this device were 81.93% and 87.57%, respectively, after 7000 cycles. The b-value of the storage device serves as a distinguishing factor; a supercapacitor's b-value ranges from 0.8 to 1.0, whereas that of a battery-grade device will be between 0 and 5. The b-value offers a comprehensive elucidation of the charge storage mechanism employed by this device. The b-values of the supercapattery device were measured at different potentials. According to Figure 8c, the b-values observed for voltages of 0.7 V, 0.8 V, and 0.9 V were 0.5, 0.6, and 0.7, respectively. Two essential elements of energy storage

systems are power density (P_d) and energy density (E_d). The following formulas can be utilized to compute these values:

$$E_d = \frac{Q \times \Delta V}{2 \times 3.6} \tag{4}$$

$$P_d = \frac{E \times 3600}{\Delta t} \tag{5}$$

The abbreviation "Q" represents the specific capacity, "E_d" energy density, "P_d" power density, and "t" represents the charging/discharging time. The device exhibited exceptional performance with an energy density of 34.79 Wh/kg and a power density of 1142.61 W/kg. The graphical representation in Figure 8d illustrates the relationship between energy density via power density and was also compared with the published data. This study emphasizes the benefits of MnNiS@MXene as a highly sought-after, reliable, and efficient electrode material for hybrid devices. Table 1 shows a study of the reported results compared to other published MXene-based compounds.
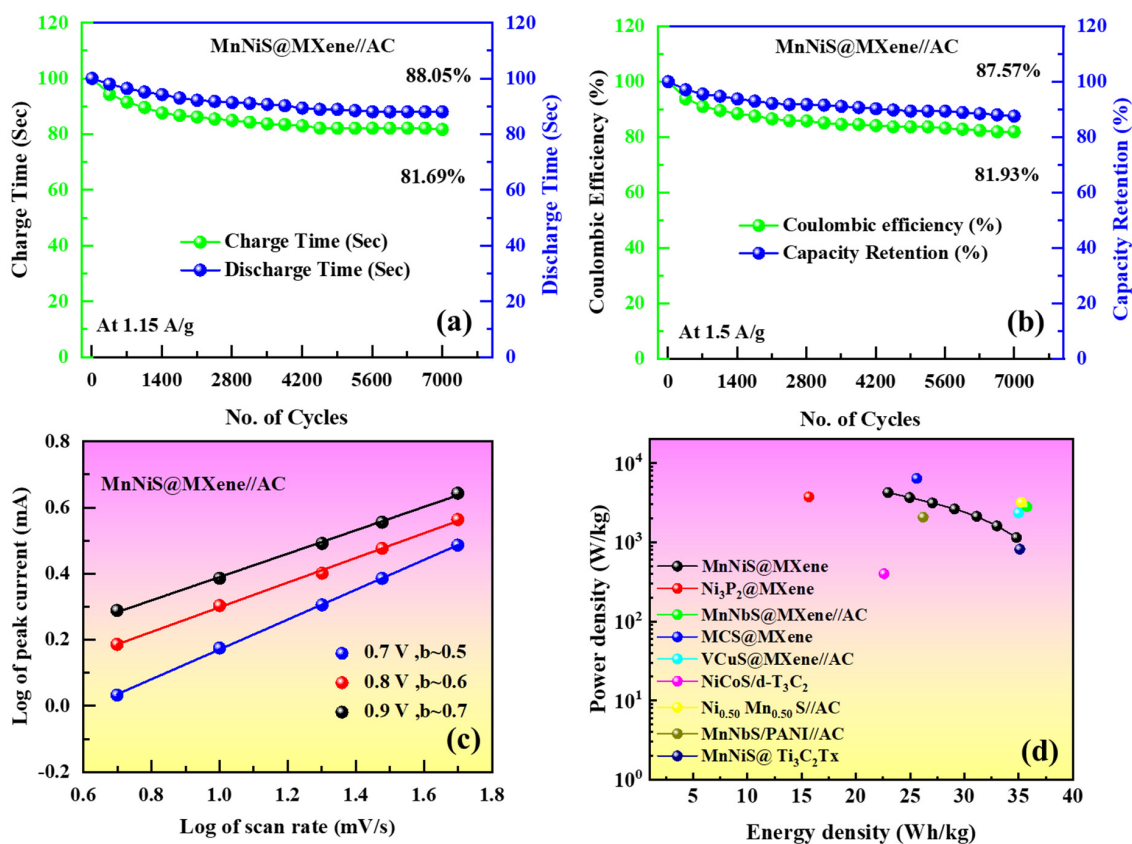

Figure 8. (**a**) Cyclic stability after 7000 GCD cycles of supercapattery device. (**b**) Capacity retention% and columbic efficiency% after 7000 cycles. (**c**) The b-value of MnNiS@MXene. (**d**) The E_d graph against P_d and comparison with the related published data.

Table 1. The comparison of the specific capacity, energy, and power densities with the related results.

Materials	Specific Capacity (C/g)	Energy Density (Wh/kg)	Power Density (W/kg)	Ref.
Ni_3P_2/MXene//AC	112.80	15.66	3748.40	[72]
MnNbS/MXene//AC	153.23	35.77	2800	[73]
MCS@MXene	600	25.6	6400	[74]
VCuS@MXene//AC	313.2	34.99	2347	[75]
NiCoS@d-T_3C_2	-	22.6	400	[76]

Materials	Specific Capacity (C/g)	Energy Density (Wh/kg)	Power Density (W/kg)	Ref.
$Ni_{0.50}Mn_{0.50}S//AC$	158.60	3524	3200	[77]
MnNbS@PANI	118.2	26.2	2072	[78]
CNT/CoMgS//AC	249.8	70.0	880	[79]
$MnNiS@Ti_3C_2Tx$	-	35.11	816.34	[80]
$MXene/MnO_2$	-	20	500	[81]
Co.Nb.S@PANI	185.0	35.0	2400	[82]
MnNiS@MXene	307.18	34.79	1142.61	This work

2.4. Photoelectrochemical Activity

Photoelectrochemical activity is the ability of a substance to create an electrical reaction when exposed to light. This feature is used in devices that combine photochemical and electrochemical principles. In the context of supercapacitors, the inclusion of photoelectrochemical activity can increase the performance by using light to promote charge storage and conversion [79,83]. Figure 9a illustrates the mechanism of the photoelectrochemical reaction, whereas Figure 9b displays the resulting photocurrent (J). The photocurrent was measured amperometrically as a current versus time profile at the open circuit potential (OCP) under conditions of chopped illumination with frequent on/off cycles. The photoelectrode composed of MnNiS@MXene exhibited remarkable photoactivity, remarkable photo-switching capabilities, and rapid reaction and recovery times. The presence of effective charge separation was demonstrated by a noticeable sudden increase during the initial light exposure, which was then followed by a rapid decrease, indicating the formation of a stable photocurrent. However, it was observed that the material exhibited limited adhesion to the ITO-glass substrate, hence posing a challenge to the long-term endurance of the photoelectrode. Enhancing our comprehension of the surface adhesion properties of MnNiS@MXene could provide valuable insights, and advancements in this field have the potential to enhance the efficiency of MnNiS@MXene as a photoelectrocatalyst.
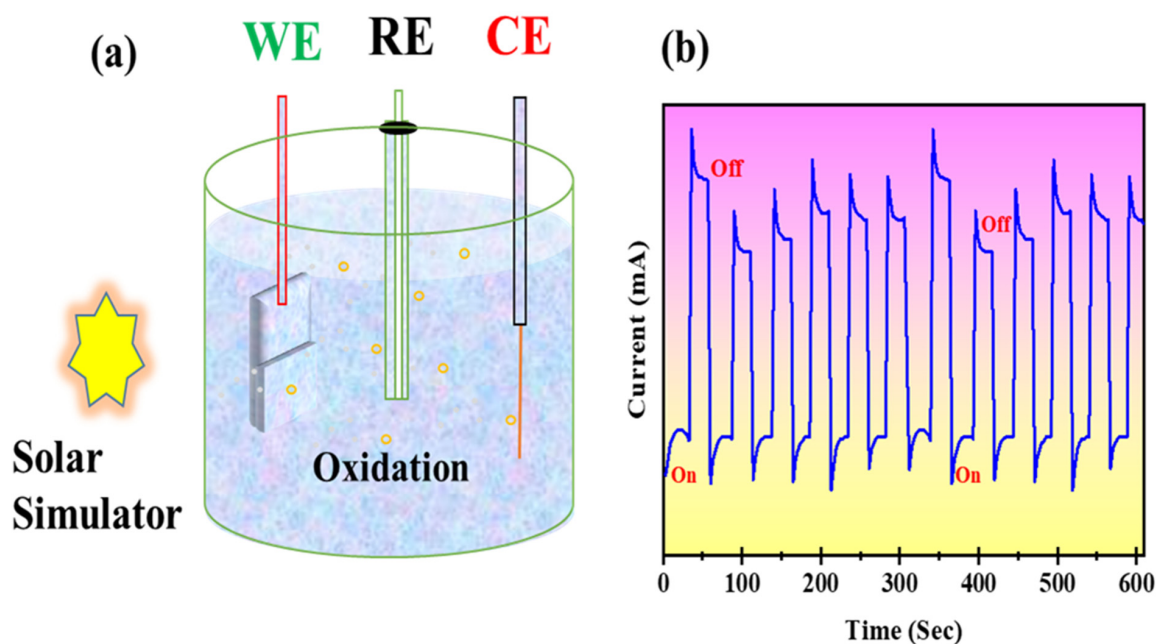

Figure 9. (**a**) Schematic of photoelectrochemical cell mechanisms. (**b**) MnNiS@MXene photoelectrode photocurrent–time profile under chopped solar light (on/off).

3. Experimental Section

3.1. Materials

A scientific supply store provided the following materials: powdered titanium aluminum carbide (Ti_3AlC_2), sodium sulfide hydrate ($Na_2S \cdot nH_2O$), lithium fluoride (LiF), potassium hydroxide (KOH), and manganese chloride ($MnCl_2$). The tea residue was gathered from some tea shops located around Pakistan. To make activated carbon (AC), it was then carbonized for 0.4 h at 800 °C, dried in an oven, and crushed in a crusher. Hydrochloric acid (HCl), N-polyvinylidene-fluoride (PVDF), carbon black (CB), and N MP were obtained from Sigma-Aldrich (St. Louis, MO, USA). Throughout the experiment, deionized water (DI) was utilized consistently for both washing and solution preparation. Without any further processing or analytical grading, all compounds were used.

3.2. Synthesis of MXene

Using a LiF and HCl combination, the MAX phase was acid etched to create HF in-situ, a safer method of synthesizing Ti_3C_2 MXene. Over 15 min, 3 g of Ti_3AlC_2 was slowly added to a pre-stirred solution of 3 g LiF and 9 M HCl. The delaminated MXene sheets were centrifuged at 3600 rpm until the pH reached 6 after being filtered through an excess of deionized (DI) water. Following synthesis, MXene was centrifuged, dried at 140 °C for 12 h, and filtered.

3.3. Synthesis of Manganese Nickel Sulfide/MXene Hybrid

Manganese chloride ($MnCl_2$) 0.40 mM, nickel chloride ($NiCl_2$) 0.40 mM, and sodium sulfide hydrate ($Na_2S.nH_2O$) 0.20 mM solutions were mixed and stirred during the synthesis process until a clear solution was achieved. After this, the solution was put into a 100 mL hydrothermal autoclave with a Teflon lining, where synthesis took place for 12 h at 130 °C. Once the finished product was cleaned with DI water, it was dried. Subsequently, 40 milliliters of deionized water were mixed with 0.2 M of $Na_2S \cdot 9H_2O$ to which the hydrothermally generated product was added. In the autoclave, the mixture was subjected to an 8-h hydrothermal reaction at 160 °C. After the reaction, the product was centrifuged with deionized water to remove unreacted components and washed with ethanol and water.

3.4. Fabrication of Electrode

Nickel foam was carefully cleaned using a series of washes in 3 mol HCl solution, ethanol, and DI water, before deposition. A homogenous slurry was prepared with 12% binder, 12% carbon black, and 76% active material. This mixture was continuously stirred for 8 h to guarantee consistency. The total loading mass of active material deposited on the nickel foam was 6 mg; in electrochemical studies carried out in a 1 M KOH electrolyte, Hg/HgO was used as the reference electrode, MnNiS@MXene as the working, and platinum wire as the counter electrode.

4. Conclusions

Finally, MnNiS@MXene, a hydrothermally generated composite, is a highly effective supercapacitor electrode material. We used SEM, XRD, and BET to assess the material's shape, crystallinity, and surface area. The formation of distinctive coral-flower-like patterns on the surface and interlayers of MXene was achieved by growing MnNiS nanoparticles in situ, resulting in this electrode. Several benefits were observed in MnNiS@MXene compared to the components used alone. With its rich mesoporous structure and huge specific surface area, it offered more active sites for metal ions. Consequently, it made the charge transmission more efficient and decreased the electrode resistance. The synergistic effect between MnNiS and MXene significantly enhanced the electrochemical performance of MnNiS@MXene. Specifically, MnNiS contributed to high specific capacitance, while MXene ensured excellent cycle stability. A comprehensive electrochemical performance examination was conducted on the produced compounds using a one molar potassium hydroxide electrolyte and a three-electrode arrangement. The specific capacity of MnNiS@MXene was

an outstanding 1189.98 C/g at 2 A/g. Activated carbon was used as the negative electrode and MnNiS@MXene as the positive electrode in a hybrid device that was assembled thereafter. With an impressive Qs of 307.18 C/g, P_d of 1142.61 W/kg, and E_d of 34.79 Wh/kg, this supercapattery demonstrated exceptional performance. Additionally, 7000 cycles of charging and discharging were used to assess the cyclic stability of the supercapattery device. The results showed that the device retained about 87.57% of its initial capacity. The aforementioned findings suggest that MnNiS@MXene exhibits promising potential as an electrode material for forthcoming energy storage systems.

Supplementary Materials: The following supporting information can be downloaded at: https://www.mdpi.com/article/10.3390/inorganics12080205/s1, Figure S1: Stability of the MnNiS@MXene electrode.

Author Contributions: Methodology, M.A., M.I., A.M.A., M.A.u.H., A.S.A., M.W.I., S.A.M.I. and H.M.H.Z.; Data curation, M.A., M.I., A.M.A., A.S.A., M.W.I., S.A.M.I. and H.M.H.Z.; Writing—original draft, A.M.A. All authors have read and agreed to the published version of the manuscript.

Conflicts of Interest: The authors declare no conflict of interest.

References

1. Wang, J.; Zhao, Y.; He, C.; Li, K.; Wang, Z.; Liu, J.; Zhang, Q.; Mao, N.; Cao, Y. Metal sulfides encapsulated in doped carbon aerogel towards superior and safe energy storage: Two birds with one stone. *Electrochim. Acta* **2024**, *477*, 143819. [CrossRef]
2. Zhang, S.; Shi, R.; Cai, K.; Wang, T.; Qu, T.; Li, L.; Lang, X. Coordination networks in accordion-like copper based metal–organic frameworks facilitate efficient catalytic strategies in high performance lithium-sulfur batteries. *J. Electroanal. Chem.* **2024**, *967*, 118468. [CrossRef]
3. Anwer, A.H.; Zubair, M.M.; Mashkoor, F.; Benamor, A.; Hasan, I.; Shoeb, M.; Jeong, C. Enhancing the electrochemical performance of hybrid supercapacitors with in-situ grown ultrasound-mediated heterostructure bi-metallic and dual-linker MOF nanoarchitecture by harnessing charge storage mechanisms. *J. Alloys Compd.* **2024**, *970*, 172512. [CrossRef]
4. Gong, Y.; Fu, D.; Fan, M.; Zheng, S.; Xue, Y. Multilayer Core–Sheath Wires with Radially Aligned N-Doped Carbon Nanohole Arrays for Boosting Energy Storage in Zinc-Ion Hybrid Supercapacitors. *ACS Appl. Mater. Interfaces* **2024**, *16*, 4793–4802. [CrossRef] [PubMed]
5. Javed, M.S.; Najam, T.; Hussain, I.; Idrees, M.; Ahmad, A.; Imran, M.; Shah, S.S.A.; Luque, R.; Han, W. Fundamentals and scientific challenges in structural design of cathode materials for zinc-ion hybrid supercapacitors. *Adv. Energy Mater.* **2023**, *13*, 2202303. [CrossRef]
6. Liang, C.; Feng, Z.; Chen, M.; Xv, X.; Lu, M.; Wang, W. Nanoflower-like hollow NiMnCo-OH decorated with self-assembled 2D Ti_3C_2Tx for high-efficiency hybrid supercapacitors. *J. Alloys Compd.* **2024**, *970*, 172537. [CrossRef]
7. Lv, Y.; Zhang, L.; Wei, X.; Qiu, B.; Zhang, W.; Qin, Q.; Jia, D.; He, X.; Liu, Z.; Wei, F. The emerging of zinc-ion hybrid supercapacitors: Advances, challenges, and future perspectives. *Sustain. Mater. Technol.* **2023**, *35*, e00536. [CrossRef]
8. Ma, N.; Yang, D.; Riaz, S.; Wang, L.; Wang, K. Aging mechanism and models of supercapacitors: A review. *Technologies* **2023**, *11*, 38. [CrossRef]
9. Ramachandran, T.; Sana, S.S.; Kumar, K.D.; Kumar, Y.A.; Hegazy, H.; Kim, S.C. Asymmetric supercapacitors: Unlocking the energy storage revolution. *J. Energy Storage* **2023**, *73*, 109096. [CrossRef]
10. Wang, W.; Yang, C.; Han, D.; Yu, S.; Qi, W.; Ling, R.; Liu, G. Ni_3S_2/Ni_2O_3 heterojunction anchored on N-doped carbon nanosheet aerogels for dual-ion hybrid supercapacitors. *J. Colloid Interface Sci.* **2024**, *654*, 709–718. [CrossRef]
11. Xiong, C.; Wang, T.; Zhao, Z.; Ni, Y. Recent progress in the development of smart supercapacitors. *SmartMat* **2023**, *4*, e1158. [CrossRef]
12. Zheng, R.; Lin, H.; Ding, J.; Zhou, P.; Ying, Y.; Liu, Y. A self-supporting multi-component collaborative structure for enhancing interface electron transfer in hybrid supercapacitor. *J. Energy Storage* **2024**, *75*, 109565. [CrossRef]
13. Bahadur, R.; Singh, G.; Li, Z.; Singh, B.; Srivastava, R.; Sakamoto, Y.; Chang, S.; Murugavel, R.; Vinu, A. Hybrid nanoarchitectonics of ordered mesoporous C60–BCN with high surface area for supercapacitors and lithium-ion batteries. *Carbon* **2024**, *216*, 118568. [CrossRef]

14. Hussain, M.; Alahmari, S.D.; Alharbi, F.; Ejaz, S.R.; Abdullah, M.; Aman, S.; Al-Sehemi, A.G.; Henaish, A.; Sadaf, A.; Farid, H.M.T. Hydrothermal synthesis of the NiS@ g-C$_3$N$_4$ nanohybrid electrode material for supercapacitor applications. *J. Energy Storage* **2024**, *80*, 110289. [CrossRef]

15. Kour, P.; Kour, S.; Sharma, A.; Yadav, K. Electrochemical Advancements in Molybdenum Disulfide via Different Transition Metal (Cr, Mn, Fe, Co) Doping for Hybrid Supercapacitors. *J. Alloys Compd.* **2024**, *981*, 173740. [CrossRef]

16. Li, C.; Jin, R.; Ke, S.; Liu, S.; Li, Q.; Liu, Q.; Zhang, Y. Sulfur vacancies reinforced cobalt molybdenum sulfide nanosheets integrated cathode for high energy density hybrid supercapacitors. *Electrochim. Acta* **2024**, *475*, 143594. [CrossRef]

17. Molaei, M.; Rostami, G.R.; Zardkhoshoui, A.M.; Davarani, S.S.H. In situ tellurization strategy for crafting nickel ditelluride/cobalt ditelluride hierarchical nanostructures: A leap forward in hybrid supercapacitor electrode materials. *J. Colloid Interface Sci.* **2024**, *653*, 1683–1693. [CrossRef] [PubMed]

18. Shembade, U.V.; Gurav, S.R.; Gaikwad, M.A.; Wategaonkar, S.B.; Ghatage, S.R.; Sonkawade, R.G.; Kim, J.H.; Moholkar, A.V. Hydrothermal synthesis of graphene oxide interspersed in non-uniform tungsten oxide nanorod and its performance towards highly efficient hybrid supercapacitor. *Ceram. Int.* **2024**, *50*, 340–350. [CrossRef]

19. Shembade, U.V.; Wategaonkar, S.B.; Moholkar, A.V. Exploring the synergistic effect of temperature on hydrothermally synthesized tungsten oxide (WO$_3$) nanostructures and its role in asymmetric liquid-state hybrid supercapacitors. *Colloids Surf. A Physicochem. Eng. Asp.* **2024**, *682*, 132916. [CrossRef]

20. Song, Z.; Wang, Z.; Yu, R. Strategies for Advanced Supercapacitors Based on 2D Transition Metal Dichalcogenides: From Material Design to Device Setup. *Small Methods* **2024**, *8*, 2300808. [CrossRef]

21. Yin, S.; Du, Y.; Liang, X.; Xie, Y.; Xie, D.; Mei, Y. Surface coating of biomass-modified black phosphorus enhances flame retardancy of rigid polyurethane foam and its synergistic mechanism. *Appl. Surf. Sci.* **2023**, *637*, 157961. [CrossRef]

22. Zhang, X.; Tang, Y.; Zhang, F.; Lee, C.-S. A novel aluminum–graphite dual-ion battery. *Adv. Energy Mater.* **2016**, *6*, 1502588. [CrossRef]

23. Wan, L.; Chen, J.; Zhang, Y.; Du, C.; Xie, M.; Hu, S. High-mass-loading cobalt iron phosphide@ nickel vanadium layered double hydroxide heterogeneous nanosheet arrays for hybrid supercapacitors. *J. Colloid Interface Sci.* **2024**, *654*, 539–549. [CrossRef] [PubMed]

24. Wang, X.; Abdurexit, A.; Jamal, R.; Abdiryim, T.; Fan, N.; Liu, Y.; Song, K.; Yang, H. Preparation of PEDOT/Ti$_3$C$_2$Tx/Co$_3$S$_2$ Composite for Quasi−Solid−State Hybrid Supercapacitor with Enhanced Electrochemical Performance. *J. Alloys Compd.* **2024**, *980*, 173609. [CrossRef]

25. Dong, W.; Xie, M.; Zhao, S.; Qin, Q.; Huang, F. Materials design and preparation for high energy density and high power density electrochemical supercapacitors. *Mater. Sci. Eng. R Rep.* **2023**, *152*, 100713. [CrossRef]

26. Fan, X.; Huang, K.; Chen, L.; You, H.; Yao, M.; Jiang, H.; Zhang, L.; Lian, C.; Gao, X.; Li, C. High Power-and Energy-Density Supercapacitors through the Chlorine Respiration Mechanism. *Angew. Chem. Int. Ed.* **2023**, *62*, e202215342. [CrossRef] [PubMed]

27. Fu, X.; Wang, J.; Peng, F.; Wang, Y.; Hu, S.; Zhang, R.; Liu, Q. A hybrid PEMFC/supercapacitor device with high energy and power densities based on reduced graphene oxide/Nafion/Pt electrode. *Int. J. Hydrogen Energy* **2023**, *48*, 16072–16082. [CrossRef]

28. Liang, C.; Wang, S.; Sha, S.; Lv, S.; Wang, G.; Wang, B.; Li, Q.; Yu, J.; Xu, X.; Zhang, L. Novel semiconductor materials for advanced supercapacitors. *J. Mater. Chem. C* **2023**, *11*, 4288–4317. [CrossRef]

29. Lim, J.M.; Jang, Y.S.; Nguyen, H.V.T.; Kim, J.S.; Yoon, Y.; Park, B.J.; Seo, D.H.; Lee, K.-K.; Han, Z.; Ostrikov, K.K. Advances in high-voltage supercapacitors for energy storage systems: Materials and electrolyte tailoring to implementation. *Nanoscale Adv.* **2023**, *5*, 615–626. [CrossRef]

30. Mondal, S.; Velpula, D.; Sangaranarayanan, M. Electrochemical supercapacitors: An overview on analysis and modeling. In *Polymer Electrolyte-Based Electrochemical Devices*; Elsevier: Amsterdam, The Netherlands, 2024; pp. 255–282.

31. Qin, G.; Wu, C.; Song, X.; He, W.; Yang, J.; Yu, X.; Chen, Q. Multifunctional enhanced energy density integrated supercapacitor based on self-healing redox-mediated gel polymer electrolyte. *Fuel* **2024**, *357*, 130033. [CrossRef]

32. Zhang, J.; Yang, H.; Huang, Z.; Zhang, H.; Lu, X.; Yan, J.; Cen, K.; Bo, Z. Pore-structure regulation and heteroatom doping of activated carbon for supercapacitors with excellent rate performance and power density. *Waste Dispos. Sustain. Energy* **2023**, *5*, 417–426. [CrossRef]

33. Wang, M.; Jiang, C.; Zhang, S.; Song, X.; Tang, Y.; Cheng, H.-M. Reversible calcium alloying enables a practical room-temperature rechargeable calcium-ion battery with a high discharge voltage. *Nat. Chem.* **2018**, *10*, 667–672. [CrossRef]

34. Guo, X.; Peng, Q.; Shin, K.; Zheng, Y.; Tunmee, S.; Zou, C.; Zhou, X.; Tang, Y. Construction of a Composite Sn-DLC Artificial Protective Layer with Hierarchical Interfacial Coupling Based on Gradient Coating Technology Toward Robust Anodes for Zn Metal Batteries. *Adv. Energy Mater.* **2024**, 2402015. [CrossRef]

35. Xu, X.; Dong, Y.; Hu, Q.; Si, N.; Zhang, C. Electrochemical hydrogen storage materials: State-of-the-art and future perspectives. *Energy Fuels* **2024**, *38*, 7579–7613. [CrossRef]

36. Liu, P.; Song, Z.; Miao, L.; Lv, Y.; Gan, L.; Liu, M. Boosting Spatial Charge Storage in Ion-Compatible Pores of Carbon Superstructures for Advanced Zinc-Ion Capacitors. *Small* **2024**, 2400774. [CrossRef]

37. Mansuer, M.; Miao, L.; Qin, Y.; Song, Z.; Zhu, D.; Duan, H.; Lv, Y.; Li, L.; Liu, M.; Gan, L. Trapping precursor-level functionalities in hierarchically porous carbons prepared by a pre-stabilization route for superior supercapacitors. *Chin. Chem. Lett.* **2023**, *34*, 107304. [CrossRef]

38. Imran, M.; Ahmad, M.; Yasmeen, A.; Afzal, A.M.; Iqbal, M.W.; Mumtaz, S.; Iqbal, M.Z.; Yusuf, K.; Munnaf, S.A.; Mumtaz, M.A. Synergistic Advancements in Battery-Grade Energy Storage: AgCoS@ MXene@ AC Hybrid Electrode Material as an Enhanced Electrocatalyst for Oxygen Reduction Reaction. *ECS J. Solid State Sci. Technol.* **2024**, *13*, 071004. [CrossRef]

39. Pan, L.; Wang, F.; He, Y.; Sun, X.; Du, G.; Zhou, Q.; Zhang, J.; Zhang, Z.; Li, J. Reassessing self-healing in metallized film capacitors: A focus on safety and damage analysis. In *IEEE Transactions on Dielectrics and Electrical Insulation*; IEEE: Piscataway, NJ, USA, 2024.

40. Imran, M.; Afzal, A.M.; Iqbal, M.W.; Mumtaz, S.; Alqarni, A.S. Superior Electrochemical Performance and Cyclic Stability of WS2@ CoMgS//AC Composite on the Nickel-Foam for Asymmetric Supercapacitor Devices. *Energies* **2024**, *17*, 3363. [CrossRef]

41. Zhao, H.; Zhao, G.; Liu, F.; Xiang, T.; Zhou, J.; Li, L. Realizing dendrite-free lithium deposition with three-dimensional soft-rigid nanofiber interlayers. *J. Colloid Interface Sci.* **2024**, *666*, 131–140. [CrossRef]

42. Liu, Y.; Liu, X.; Li, X.; Yuan, H. Analytical Model and Safe-Operation-Area Analysis of Bridge-Leg Crosstalk of GaN E-HEMT Considering Correlation Effect of Multi-Parameters. *IEEE Trans. Power Electron.* **2024**, *39*, 8146–8161. [CrossRef]

43. Varghese, S.M.; Mohan, V.V.; Suresh, S.; Gowd, E.B.; Rakhi, R. Synergistically modified Ti_3C_2Tx MXene conducting polymer nanocomposites as efficient electrode materials for supercapacitors. *J. Alloys Compd.* **2024**, *973*, 172923. [CrossRef]

44. Pathak, M.; Bhatt, D.; Bhatt, R.C.; Bohra, B.S.; Tatrari, G.; Rana, S.; Arya, M.C.; Sahoo, N.G. High Energy Density Supercapacitors: An Overview of Efficient Electrode Materials, Electrolytes, Design, and Fabrication. *Chem. Rec.* **2024**, *24*, e202300236. [CrossRef]

45. Iro, Z.S.; Subramani, C.; Dash, S. A brief review on electrode materials for supercapacitor. *Int. J. Electrochem. Sci* **2016**, *11*, 10628–10643. [CrossRef]

46. Radhakrishnan, S.; Patra, A.; Manasa, G.; Belgami, M.A.; Mun Jeong, S.; Rout, C.S. Borocarbonitride-Based Emerging Materials for Supercapacitor Applications: Recent Advances, Challenges, and Future Perspectives. *Adv. Sci.* **2024**, *11*, 2305325. [CrossRef]

47. Chen, D.; Li, Y.; Li, X.; Hong, X.; Fan, X.; Savidge, T. Key difference between transition state stabilization and ground state destabilization: Increasing atomic charge densities before or during enzyme–substrate binding. *Chem. Sci.* **2022**, *13*, 8193–8202. [CrossRef]

48. Yin, C.; Zhang, T.; Zhang, C.; Zhang, Y.; Jeong, C.K.; Hwang, G.T.; Chi, Q. Flexible mica films coated by magnetron sputtered insulating layers for high-temperature capacitive energy storage. *SusMat* **2024**, e228. [CrossRef]

49. Alam, S.; Fiaz, M.I.K.F.; Iqbal, M.Z.; Alam, F.; Ahmad, Z.; Hegazy, H.H. Advancements in asymmetric supercapacitors: Material selection, mechanisms, and breakthroughs with metallic oxides, sulfides, and phosphates. *J. Energy Storage* **2023**, *72*, 108208. [CrossRef]

50. Song, X.; Zhong, R.; Zeng, Y.; Wu, X.; Tan, L. Cobalt nickel sulfide anchored on graphene for high performance all-solid-state asymmetric supercapacitors. *Diam. Relat. Mater.* **2023**, *140*, 110447. [CrossRef]

51. Melkiyur, I.; Rathinam, Y.; Kumar, P.S.; Sankaiya, A.; Pitchaiya, S.; Ganesan, R.; Velauthapillai, D. A comprehensive review on novel quaternary metal oxide and sulphide electrode materials for supercapacitor: Origin, fundamentals, present perspectives and future aspects. *Renew. Sustain. Energy Rev.* **2023**, *173*, 113106. [CrossRef]

52. Ahmad, F.; Khan, M.A.; Waqas, U.; Ramay, S.M.; Atiq, S. Elucidating an efficient super-capacitive response of a $Sr_2Ni_2O_5$/Rgo composite as an electrode material in supercapacitors. *RSC Adv.* **2023**, *13*, 25316–25326. [CrossRef]

53. Iqbal, M.Z.; Aziz, U.; Amjad, N.; Aftab, S.; Wabaidur, S.M. Porous activated carbon and highly redox active transition metal sulfide by employing multi-synthesis approaches for battery-supercapacitor applications. *Diam. Relat. Mater.* **2023**, *136*, 110019. [CrossRef]

54. Singh, P.N.; Mohamed, M.G.; Chaganti, S.V.; Sharma, S.U.; Ejaz, M.; Lee, J.-T.; Kuo, S.-W. Rational design of ultrastable conjugated microporous polymers based on pyrene and perylene units as high-performance organic electrode materials for supercapacitor applications. *ACS Appl. Energy Mater.* **2023**, *6*, 8277–8287. [CrossRef]

55. Ali, Z.; Iqbal, M.Z.; Hegazy, H. Recent advancements in redox-active transition metal sulfides as battery-grade electrode materials for hybrid supercapacitors. *J. Energy Storage* **2023**, *73*, 108857. [CrossRef]

56. Wei, S.; Wan, C.; Wu, Y. Recent advances in wood-based electrode materials for supercapacitors. *Green Chem.* **2023**, *25*, 3322–3353. [CrossRef]

57. Wang, X.; Luo, Z.; Huang, J.; Chen, Z.; Xiang, T.; Feng, Z.; Wang, J.; Wang, S.; Ma, Y.; Yang, H. S/N-co-doped graphite nanosheets exfoliated via three-roll milling for high-performance sodium/potassium ion batteries. *J. Mater. Sci. Technol.* **2023**, *147*, 47–55. [CrossRef]

58. Rajasekaran, S.; KR, S.D.; Reghunath, B.S.; Saravanakumar, B.; William, J.J.; Pinheiro, D. Sm-MOF/rGO/PANI composite as an electrode material for supercapacitor applications. *Electrochim. Acta* **2023**, *467*, 143031. [CrossRef]

59. Iqbal, M.Z.; Ullah, A.; Aziz, U.; Asif, M.; Wabaidur, S.M.; Ansari, M.Z. Unveiling the performance of hydrothermally synthesized transition metal sulfide with polyaniline composite for hybrid supercapacitor applications. *Curr. Appl. Phys.* **2023**, *52*, 94–100. [CrossRef]

60. Zhu, X.-D.; Ren, C.-Y.; Liang, Y.; Liang, X.; Lu, N.; Zhang, Y.-C.; Zhao, Y.; Gao, J. Laser-assisted one-step fabrication of interlayer-spacing-regulated three-dimensional MXene-based micro-supercapacitors. *Chem. Eng. J.* **2024**, *483*, 149253. [CrossRef]

61. Zhou, G.; Liu, X.; Liu, C.; Li, Z.; Liu, C.; Shi, X.; Li, Z.; Mei, C.; Li, M.-C. 3D printed MXene-based films and cellulose nanofiber reinforced hydrogel electrolyte to enable high-performance flexible supercapacitors. *J. Mater. Chem. A* **2024**, *12*, 3734–3744. [CrossRef]

62. Xu, H.; Chen, Y.; Wen, Q.; Lin, C.; Gao, H.; Qiu, Z.; Yang, L.; Pan, X. Electrostatic self-assembled nickel cobalt sulfide/Ti_3C_2 Mxene as a bio-capacitive anode for specific attracting sulfur-cycling bacteria and regulating extracellular electron transfer efficiency. *J. Clean. Prod.* **2024**, *436*, 140595. [CrossRef]

63. Tang, J.; Zheng, X.; Ding, B.; Zou, L.; Wang, P.; Li, C.; Hong, X.; Wang, Z. MXene/PANI composite fiber-based asymmetric supercapacitors for self-powered energy storage system. *Mater. Lett.* **2024**, *355*, 135494. [CrossRef]

64. Shafique, R.; Rani, M.; Batool, K.; Shah, A.A.; Bahajjaj, A.A.A.; Sillanpää, M.; Alsalmah, H.A.; Janjua, N.K.; Arshad, M. Nanoengineering of novel MXene (Ti_3C_2Tx) based $MgCr_2O_4$ nanocomposite with detailed synthesis, morphology and characterization for enhanced energy storage application. *Mater. Sci. Eng. B* **2024**, *299*, 117036. [CrossRef]

65. Padha, B.; Verma, S.; Ahmed, A.; Patole, S.P.; Arya, S. Plastic turned into MXene–based pyro-piezoelectric hybrid nanogenerator-driven self-powered wearable symmetric supercapacitor. *Appl. Energy* **2024**, *356*, 122402. [CrossRef]

66. Mubeen, I.; Shah, S.; Pervaiz, E.; Miran, W. The promising frontier for next-generation energy storage and clean energy production: A review on synthesis and applications of MXenes. *Mater. Sci. Energy Technol.* **2024**, *7*, 180–194. [CrossRef]

67. Khan, M.S.; Imran, M.; Afzal, A.M.; Iqbal, M.W.; Mumtaz, S.; Alotaibi, N.H.; Mohammad, S. Fabrication and evaluation of VNbS@ MXene@ AC//NF composite electrodes for advanced energy storage and biomedical applications. *Mater. Sci. Eng. B* **2024**, *308*, 117569. [CrossRef]

68. Hussain, I.; Amara, U.; Bibi, F.; Hanan, A.; Lakhan, M.N.; Soomro, I.A.; Khan, A.; Shaheen, I.; Sajjad, U.; Rani, G.M. Mo-based MXenes: Synthesis, properties, and applications. *Adv. Colloid Interface Sci.* **2024**, *324*, 103077. [CrossRef]

69. Miranda, M.; Sasaki, J.J.A.C.S.A.F. The limit of application of the Scherrer equation. *Acta Crystallogr. A Found. Adv.* **2018**, *74*, 54–65. [CrossRef]

70. Imran, M.; Khan, R.; Afzal, A.M.; Iqbal, M.W.; Mumtaz, S.; Iqbal, M.Z.; Zhang, X.; Ali, A.; Albaqami, M.D.; Mohammad, S. Designing high-performance hybrid supercapacitors and electrochemical sensors with carbon nanotube-embedded silver manganese sulfide@AC@NF composites. *J. Energy Storage* **2024**, *96*, 112642. [CrossRef]

71. Khan, R.; Imran, M.; Afzal, A.M.; Iqbal, M.W.; Mumtaz, S.; Bahajjaj, A.A.A.; Ahmad, A.u.; Munnaf, S.A.; Choi, E.H.; Subhani, W.S.; et al. Synthesis of binder-free MgSrS/CNT nanocomposite and measure the electrochemical characteristics of asymmetric supercapacitor. *J. Mater. Sci. Mater. Electron.* **2024**, *35*, 386. [CrossRef]

72. Venkateshalu, S.; Cherusseri, J.; Karnan, M.; Kumar, K.S.; Kollu, P.; Sathish, M.; Thomas, J.; Jeong, S.K.; Grace, A.N. New Method for the Synthesis of 2D Vanadium Nitride (MXene) and Its Application as a Supercapacitor Electrode. *ACS Omega* **2020**, *5*, 17983–17992. [CrossRef]

73. Hussain, Z.; Imran, M.; Afzal, A.M.; Iqbal, M.W.; Mumtaz, S.; Munnaf, S.A.; Wabaidur, S.M.; Fatima, W.; Safdar, S.; Mumtaz, M.A.; et al. High performance MnNbS@MXene hybrid electrode for battery-supercapacitor hybrid device and biomedical applications. *Mater. Sci. Semicond. Process.* **2024**, *173*, 108091. [CrossRef]

74. Nasrin, K.; Subramani, K.; Karnan, M.; Sathish, M. $MnCo_2S_4$–MXene: A novel hybrid electrode material for high performance long-life asymmetric supercapattery. *J. Colloid Interface Sci.* **2021**, *600*, 264–277. [CrossRef]

75. Muzaffar, N.; Anjam, N.; Imran, M.; Afzal, A.M.; Iqbal, M.W.; Alotaibi, N.H.; Mohammad, S.; Mumtaz, S.; Hassan, A.M.; Ahmad, Z.; et al. Designing of VCuS@MXene nanocomposite electrode for energy storage device and electrochemical glucose sensor. *J. Mater. Sci. Mater. Electron.* **2024**, *35*, 661. [CrossRef]

76. Luo, Y.; Tian, Y.; Tang, Y.; Yin, X.; Que, W. 2D hierarchical nickel cobalt sulfides coupled with ultrathin titanium carbide (MXene) nanosheets for hybrid supercapacitors. *J. Power Sources* **2021**, *482*, 228961. [CrossRef]

77. Imran, M.; Iqbal, M.W.; Afzal, A.M.; Faisal, M.M.; Alzahrani, H.A. Synergetic electrochemical performance of Nix–Mnx sulfide-based binary electrode material for supercapattery devices. *J. Appl. Electrochem.* **2023**, *53*, 1125–1136. [CrossRef]

78. Khan, R.; Afzal, A.M.; Hussain, Z.; Iqbal, M.W.; Imran, M.; Hamza Waris, M.; Azhar Mumtaz, M.; Usman, M.; Wabaidur, S.M.; Al-Ammar, E.A.; et al. MnNbS/Polyaniline Composite-Based Electrode Material for High-Performance Energy Storage Hybrid Supercapacitor Device. *Phys. Status Solidi* **2023**, *220*, 2300200. [CrossRef]

79. Imran, M.; Afzal, A.M.; Safdar, S.; Muzaffar, N.; Iqbal, M.W.; Naz, A.; Albaqami, M.D.; Mohammad, S.; Mumtaz, S.; Ahmad, Z. Enhancing the electrochemical and photoelectrochemical effects in CNTs@CoMgS@AC nanocomposite based electrode materials for advanced hybrid supercapacitors. *Mater. Sci. Eng. B* **2024**, *300*, 117138. [CrossRef]

80. Hu, P.; Chai, R.; Wang, P.; Yang, J.; Zhou, S. Supercapacitive properties of $MnNiSx@Ti_3C_2Tx$ MXene positive electrode assisted by functionalized ionic liquid. *Chin. J. Chem. Eng.* **2023**, *61*, 102–109. [CrossRef]

81. Zhu, Y.; Rajouâ, K.; Le Vot, S.; Fontaine, O.; Simon, P.; Favier, F. MnO_2-MXene composite as electrode for supercapacitor. *J. Electrochem. Soc.* **2022**, *169*, 030524. [CrossRef]

82. Afzal, A.M.; Iqbal, M.W.; Imran, M.; Umair, H.; Wabaidur, S.M.; Al-Ammar, E.A.; Mumtaz, S.; Choi, E.H. Synthesis of CoNbS, PANI@CoNbS, and PANI@AC Composite and Study of the Impact of PANI on the Electrochemical Characteristics of Energy Storage Device. *ECS J. Solid State Sci. Technol.* **2023**, *12*, 051003. [CrossRef]

83. Imran, M.; Muhammad, Z.; Muzafar, N.; Afzal, A.M.; Iqbal, M.W.; Mumtaz, S.; Munnaf, S.A.; Albaqami, M.D.; Ahmad, Z. Enhanced the electrochemical performance of CoMgS nanocomposite electrode with the doping of ZnO for supercapacitor-battery hybrid device and photochemical activity. *J. Appl. Electrochem.* **2024**, *54*, 1501–1515. [CrossRef]